Impacts of Truncation Error for Near Field Antenna Assessment

M. Salucci, N. Anselmi, and A. Massa

2024/04/19

Contents

1   Planar Measurement set-up

For the performed analysis:

- the measurement points are distributed in a plane placed a certain distance away from the *AUT* along the z-axis;

- the employed *AUT* is characterized by a magnitude failure and phase shift affecting the 3rd row ($\nu^{(3)} = 0.45$, $\gamma^{(3)} = \frac{\pi}{3}$) and incremented failure ranges to build the over-complete basis ($\nu^{(s)} \in [0.0, \, 1.0]$, $F^{(s)} = 7$ and $\gamma^{(s)} \in [-\pi, \, \pi]$, $P^{(s)} = 5$) are considered. All the main parameters used for the simulations are listed below:

Parameters

Gold Antenna (Without Defects)

- Geometry : Planar array of microstrip patches on the (x, y) plane;

- Working Frequency : $f = 3.6 \, [GHz]$ ($\lambda = 83.27 \times 10^{-3} \, [m]$ in free space);

- Substrate (PEC-backed) :

    - Dimensions : infinite;

    - Relative Permittivity : $\varepsilon_{r,sub} = 4.7$;

    - Loss Tangent : $tan \, \delta_{sub} = 0.014$;

    - Thickness : $h_{sub} = 0.019 \, [\lambda]$ ($1.6 \, [mm]$);

- Microstrip patches :

    - Dimensions : $l_x \approx 0.22 \, [\lambda]$ ($18.16 \, [mm]$), $l_y \approx 0.33 \, [\lambda]$ ($27.25 \, [mm]$);

    - Feeding : pin-fed;

- Spacing between elements : $d_x = d_y = \frac{\lambda}{2}$;

- Number of elements in each row : $N_x = 6$;

- Number of elements in each column : $N_y = 10$;

- Total number of elements : $N = (N_x \times N_y) = 60$;

- Total size of the antenna : $L_x = 5 \, [\lambda]$, $L_y = 9 \, [\lambda]$;

- Element excitations : $w_n^{(s)} = 1.0 + j0.0$, $n = 1, ..., N^{(s)}$, $s = 1, ..., S$;

Antenna Under Test (AUT - With Defects)

1. Failures of the excitation magnitude of the 3rd row;

    - Failure factor of the elements in the 3rd row ($s = 3$) : $\nu^{(3)} = 0.45$;

2. Failures of the excitation phase of the 3rd row;

- Phase shift of the elements in the 3rd row $(s = 3) : \gamma^{(3)} = \frac{\pi}{3}\,[rad]$;
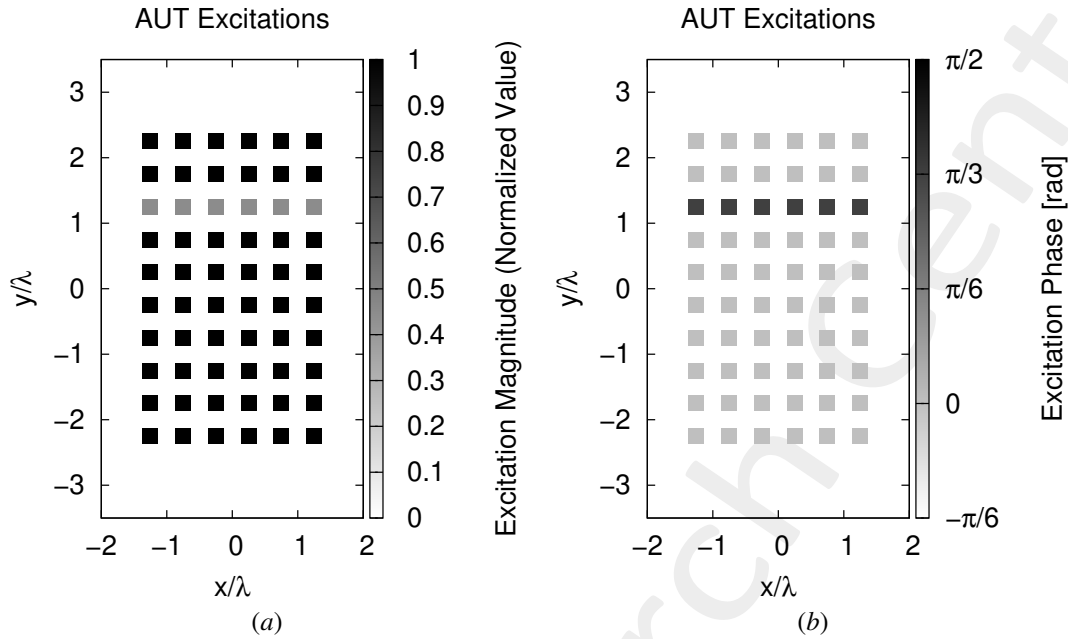

Figure 1: (*a*) Magnitude of the element excitations in the *AUT* ($\nu^{(3)} = 0.45$), (*b*) phase of the element excitations in the *AUT* ($\gamma^{(3)} = \frac{\pi}{3}\,[rad]$).

Measurement-by-Design Technique

- Number of generated bases : $B = 20$;

- Bases $b = 1, ..., 10$: magnitude failures in each row $(s = 1, ..., 10)$

  - Failure factor of the elements : $\nu^{(s)} \in [0.0,\ 1.0],\ s = 1, ..., 10$;

  - Number of simulated failure factors : $F^{(s)} = 7,\ s = 1, ..., 10$;

- Bases $b = 11, ..., 20$: phase failures in each row $(s = 1, ..., 10)$

  - Phase shift of the elements : $\gamma^{(s)} \in [-\pi,\ \pi]\,[rad],\ s = 1, ..., 10$;

  - Number of simulated phase shifts: $P^{(s)} = 5,\ s = 1, .., 10$;

- Threshold on the singular values magnitude (normalized) : $\eta = -40\,[dB]$;

- Total number of simulated *AUT* configurations : $K = S \times (F^{(s)} + P^{(s)}) = 10 \times (7 + 5) = 120$;

Dimension of the Over-Complete Basis

The dimension of the over-complete basis is

$$Q = 40$$

This number is given by the sum of the vectors belonging to the two considered bases:

1. Magnitude failures : $Q_1, ..., Q_{10} = 2$;

2. Phase failures : $Q_{11}, ..., Q_{20} = 2$.

Alternative (*BCS*) MbD parameters

- Toleration factor for *BCS* solver: $Tolerance = 1 \times 10^{-8}$;

- Initial noise variance for *BCS* solver: $\eta_0^{opt} = 10^{-2}$. This values have been obtained as a result of a calibration procedure;

Noise

- SNR on the measured data : $SNR = \{50; 40; 30; 20; 10\} [dB]$;

- Noise seed : $Noise\_Seed = 11$.

1.1 Measurement plane reduced by considering only $M = 9$ measurement points

For this test case the original measurement plane dimension ($\zeta_{meas} = 20 [\lambda]$) is considered but among all $M = 25$ measurement points just a subset $M = 9$ of them is considered. Basically, the measurements points in the outer perimeter of the measurement plane are not used to collect data. In particular this test case is characterized by the following parameters:
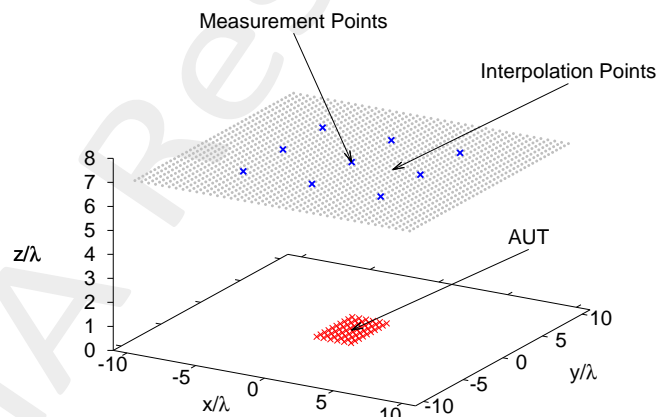
Measurement Set-Up

Figure 2: Disposition of the interpolation points ($T = 1681$) and of the measurement points ($M = 9$) in the near-field region of the *AUT*

- Type of measurements : near-field;

- Height of the measurement region : $H = 7 [\lambda]$;

- Interpolation points :

    – Number of points : $T = 41 \times 41 = 1681$;

– Coordinates : $x_t \in [-10, 10] [\lambda]$, $y_t \in [-10, 10] [\lambda]$, $z_t = H [\lambda]$, $t = 1, ..., T$;

– Interpolation step : $\Delta_{x/y}^{int} = 0.5 [\lambda]$;

• Measurement points :

  – Coordinates : $x_m^{meas} \in [-10, 10] [\lambda]$, $y_m^{meas} \in [-10, 10] [\lambda]$, $z_m^{meas} = H [\lambda]$, $m = 1, ..., M$;

  – **Number of points** : $M_{x/y} = 3 \rightarrow M = 9$;

  – Measurement step : $\Delta_{x/y}^{meas} = 5 [\lambda]$

  – **Ratio between number of measurements and total number of elements** : $(M/N) = 0.15$;

Original (*OMP*) MbD parameters

• Max. number of iterations of the OMP algorithm : $I = \{1; 2; 3; ...; 10\}$;

• Selected iteration to report the results: $I = 7$; this choice is justified by the fact that at this iteration the *OMP* algorithm reaches the best near field error as shown in the following Fig. 3.
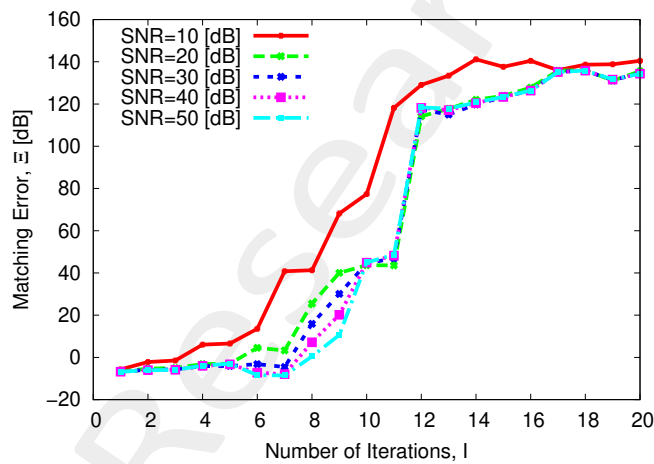

Figure 3: Behaviour of the near-field matching error versus the number of *OMP* iterations, I.

Evaluation of the Truncation Error from Actual Near-Field Data

In order to evaluate the truncation error, in the following figure is predented a visual comparison of the near-field radiated by the *AUT* measured over the full interpolation plane (ζ_{int}) and on the truncated region (ζ_{meas}), as well as the corresponding far-field patterns obtained with NF-FF transformation. The truncated near-field has been obtained as follows:

$$
E_{tr}(x,y) = \begin{cases} E(x,y) & if & -\frac{\zeta_{meas}}{2} \le \tau \le \frac{\zeta_{meas}}{2} \\ 0 & otherwise \end{cases} \quad ; \quad -\frac{\zeta_{int}}{2} \le \tau \le \frac{\zeta_{int}}{2} \tag{1}
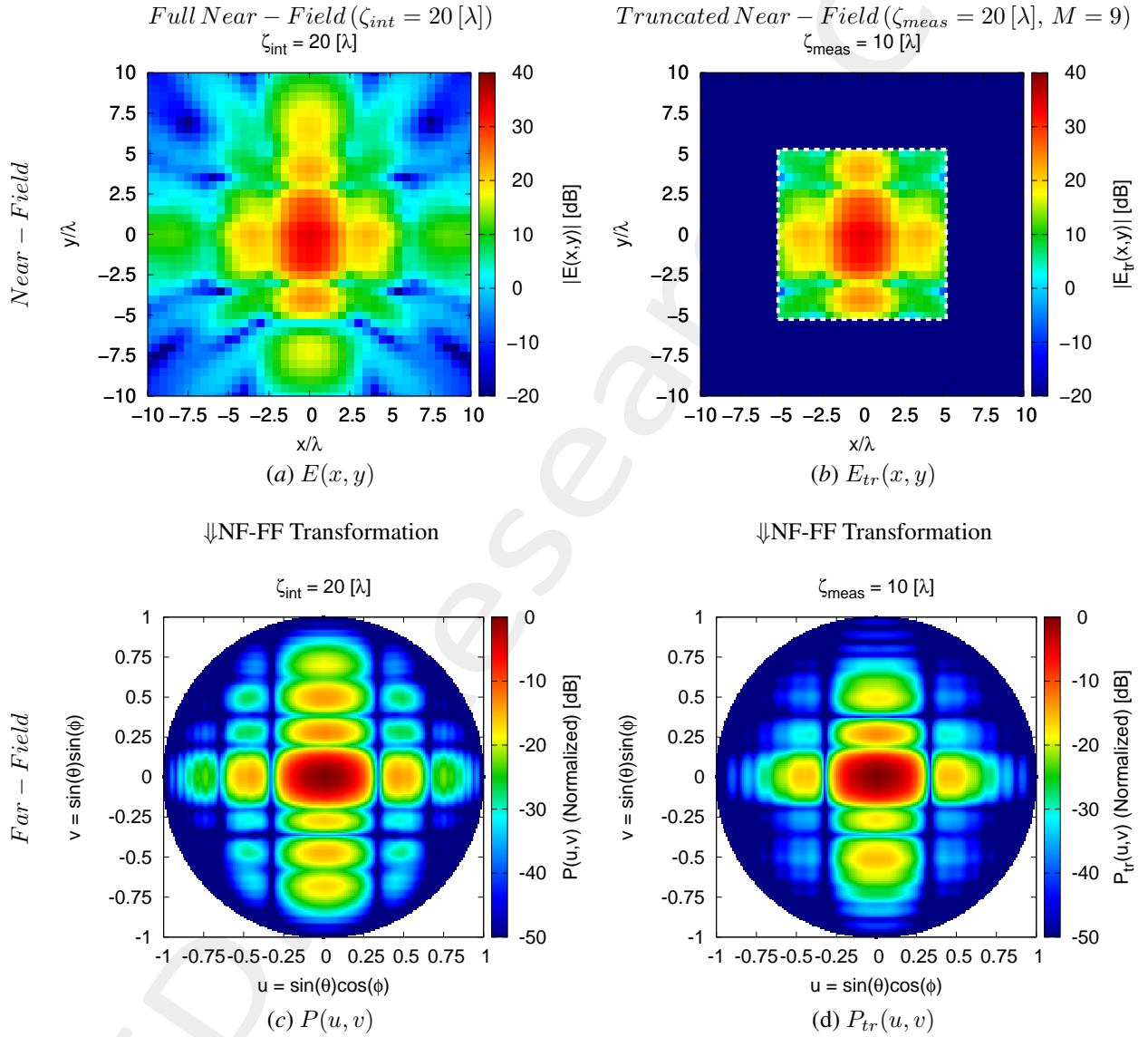$$

where $\tau = x,\, y$.

Figure 4: $\zeta_{meas} = 20\,[\lambda]$, $M = 9$ - (*a*)(*b*) Near-field and (*c*)(*d*) far-field patterns obtained via NF-FF transformation for the actual *AUT*.
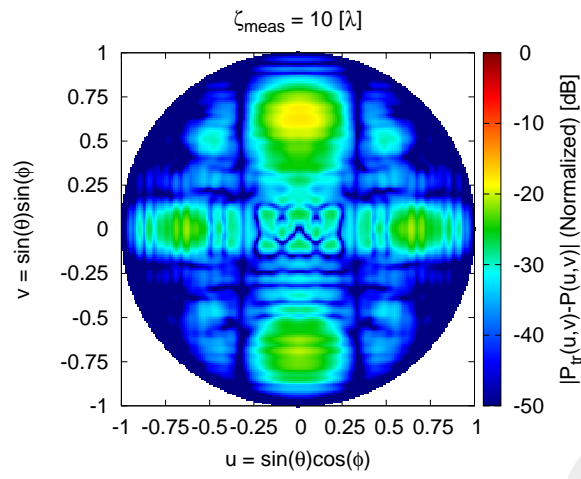
Figure 5: $\zeta_{meas} = 20\,[\lambda]$, $M = 9$ - Difference between the full and the truncated far-fields, $|P(u,v) - P_{tr}(u,v)|$.

Near-Field Error

The comparison, in terms of near field error, between the original (*OMP*) and the alternative (*BCS*) MbD is reported in the following Fig. 6:
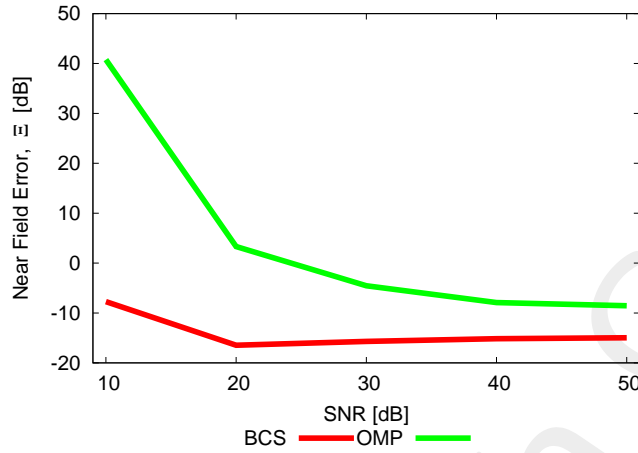

Figure 6: Near Field Error comparison between original (*OMP*) and alternative (*BCS*) MbD for different SNR values

$SNR\,[dB]$	$Near\ Field\ Error,\ \Xi\ [dB]$	
	BCS	OMP
50	-14.97	-8.55
40	-15.15	-7.92
30	-15.69	-4.55
20	-16.46	3.32
10	-7.73	40.78

Table I: Near Field Errors obtained by the original (*OMP*) and alternative (*BCS*) MbD

Observations

In the considered test case the both solvers perform poorly since the near-field error is always quite high, $\Xi > -20\,[dB]$. This means that the measurement set-up employed in this analysis does not allow to accurately reconstruct the near-field. More in details about the solvers performance:

- the *OMP* error is very high, not being able to go below $-9\,[dB]$ so that its result are the worst of the comparison;

- in general, the *BCS* results are not satisfactory because the achieved error does not allow a good near-field reconstruction; however, the BCS performance is considerably better than that of the OMP algorithm especially at low SNR values.

Estimated Near-Field
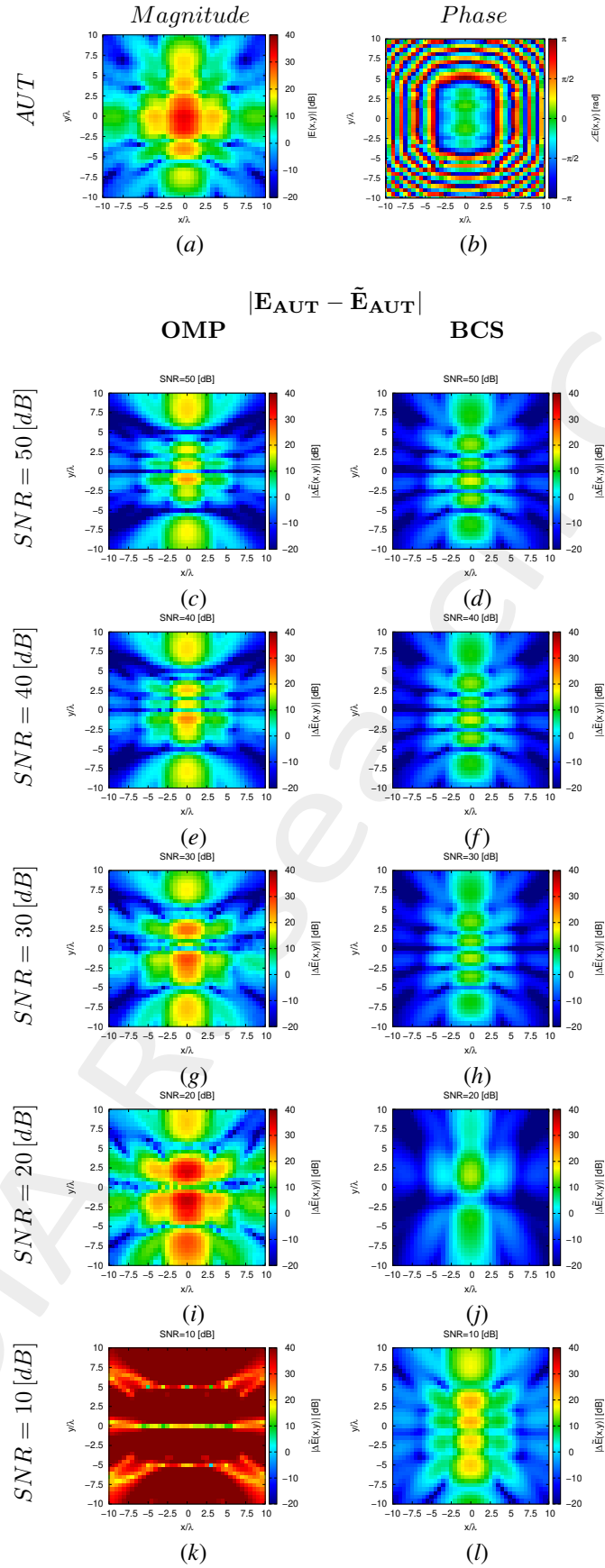

(a)   (b)

$$|\mathbf{E_{AUT}} - \tilde{\mathbf{E}}_{\mathbf{AUT}}|$$

OMP   BCS

Figure 7: Magnitude difference between the actual and estimated $2 - D$ near-field pattern when processing noisy measurements at different $SNRs$.
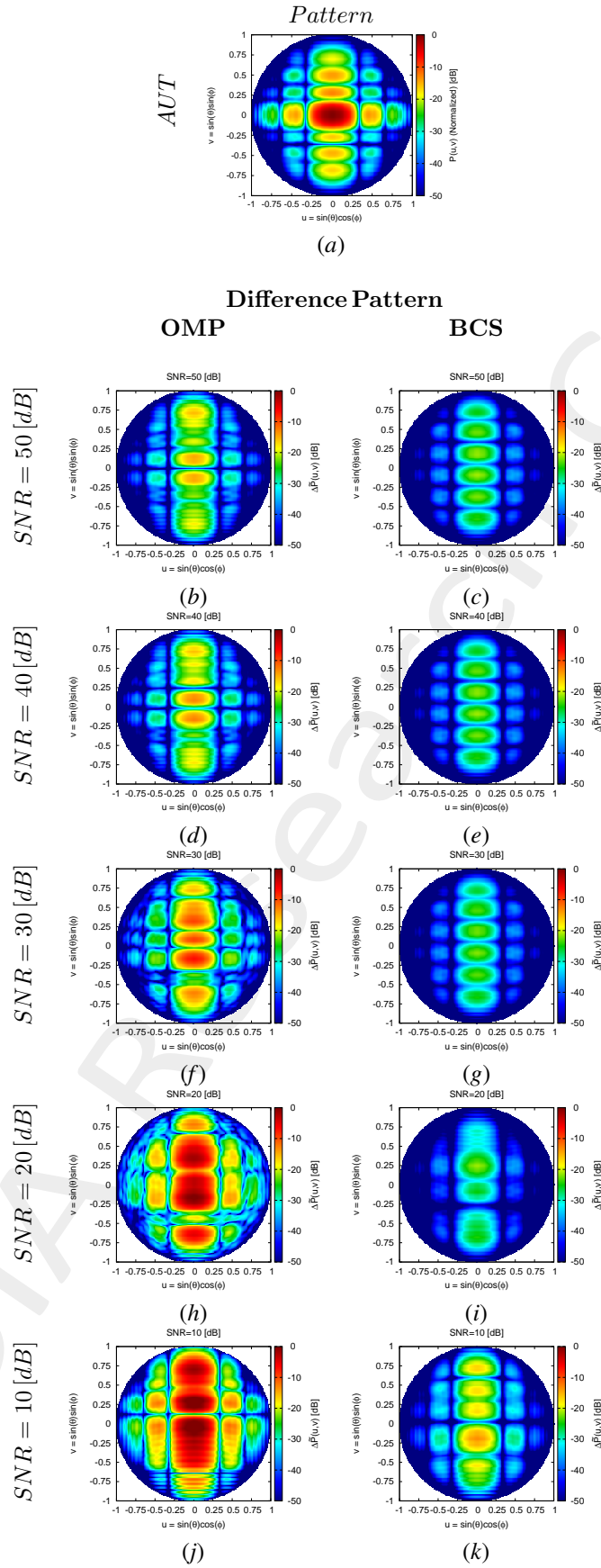
Estimated Far-Field

Figure 8: Difference between the actual and estimated $2-D$ far-field pattern when processing noisy measurements at different SNRs.

Cut @ $v = 0$

OMP　　　　　　　　　**BCS**

(a)　　　　　　　　　(b)

(c)　　　　　　　　　(d)

(e)　　　　　　　　　(f)

(g)　　　　　　　　　(h)

(i)　　　　　　　　　(j)

Figure 9: $1-D$ cuts of the estimated far-field pattern (obtained through near-to-far-field transformation from the estimated near-field patterns) under several noisy conditions
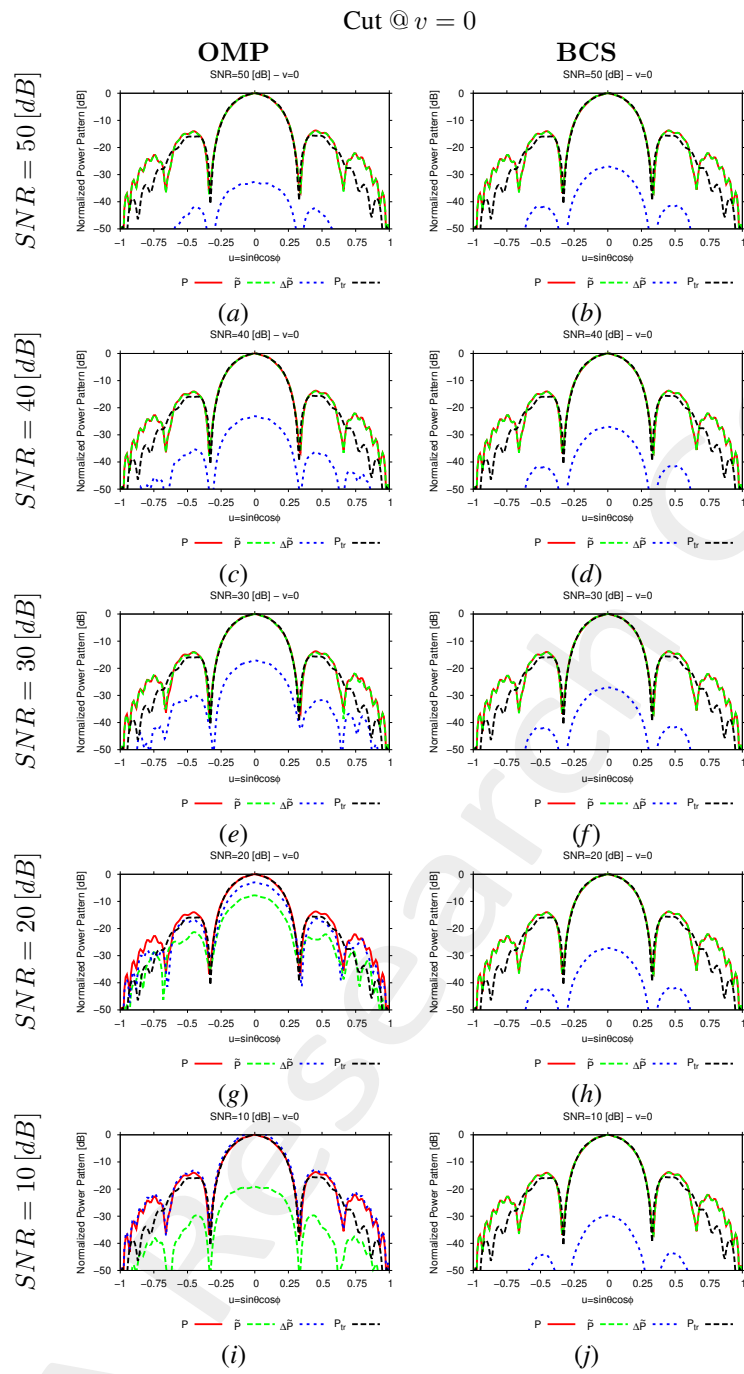
Cut @ $u = 0$

Figure 10: $1 - D$ cuts of the estimated far-field pattern (obtained through near-to-far-field transformation from the estimated near-field patterns) under several noisy conditions
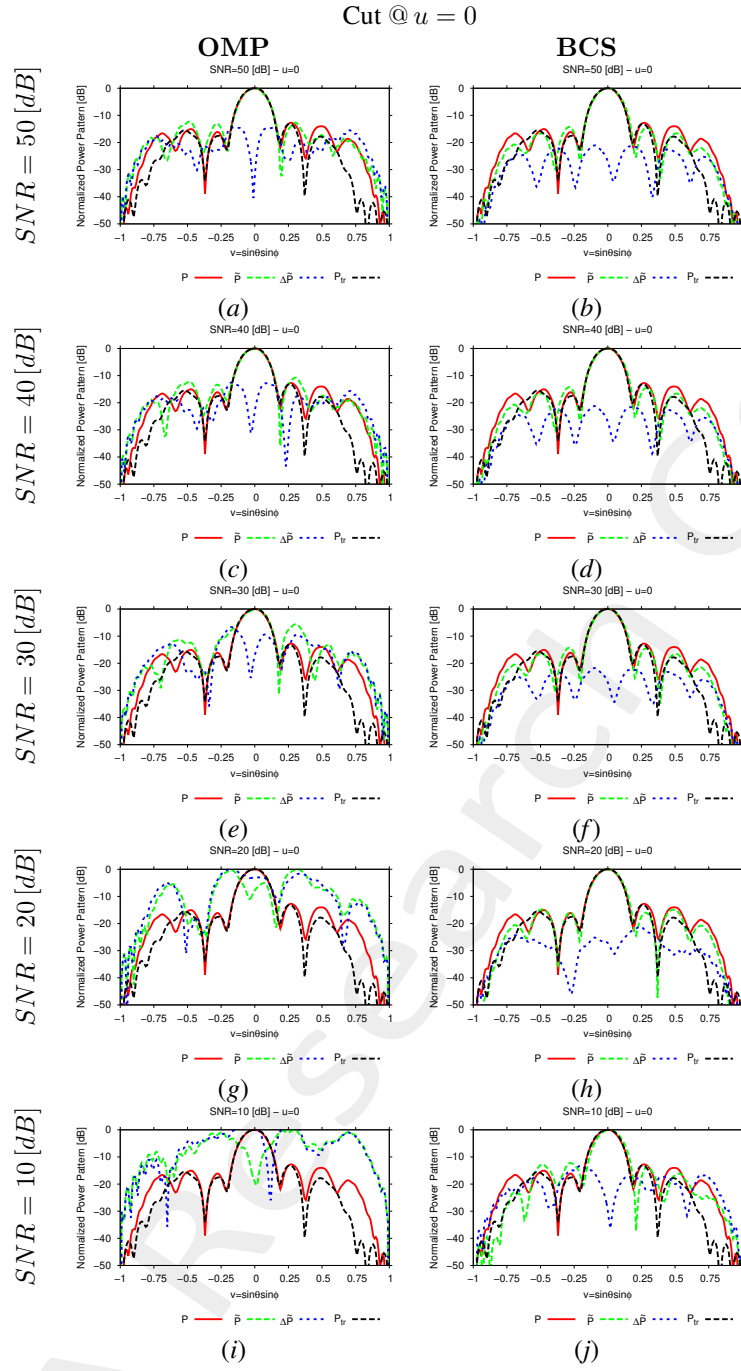
$SNR\,[dB]$	$Far - Field\ Error,\ \chi\ [dB]$	
	BCS	OMP
50	-16.11	-9.87
40	-16.25	-8.87
30	-16.69	-4.18
20	-17.83	3.86
10	-9.61	6.28

Table II: Far-field matching error between the actual and estimated AUT patterns (both obtained through near-to-far-field transformation from the corresponding near-field patterns) under several noisy conditions.
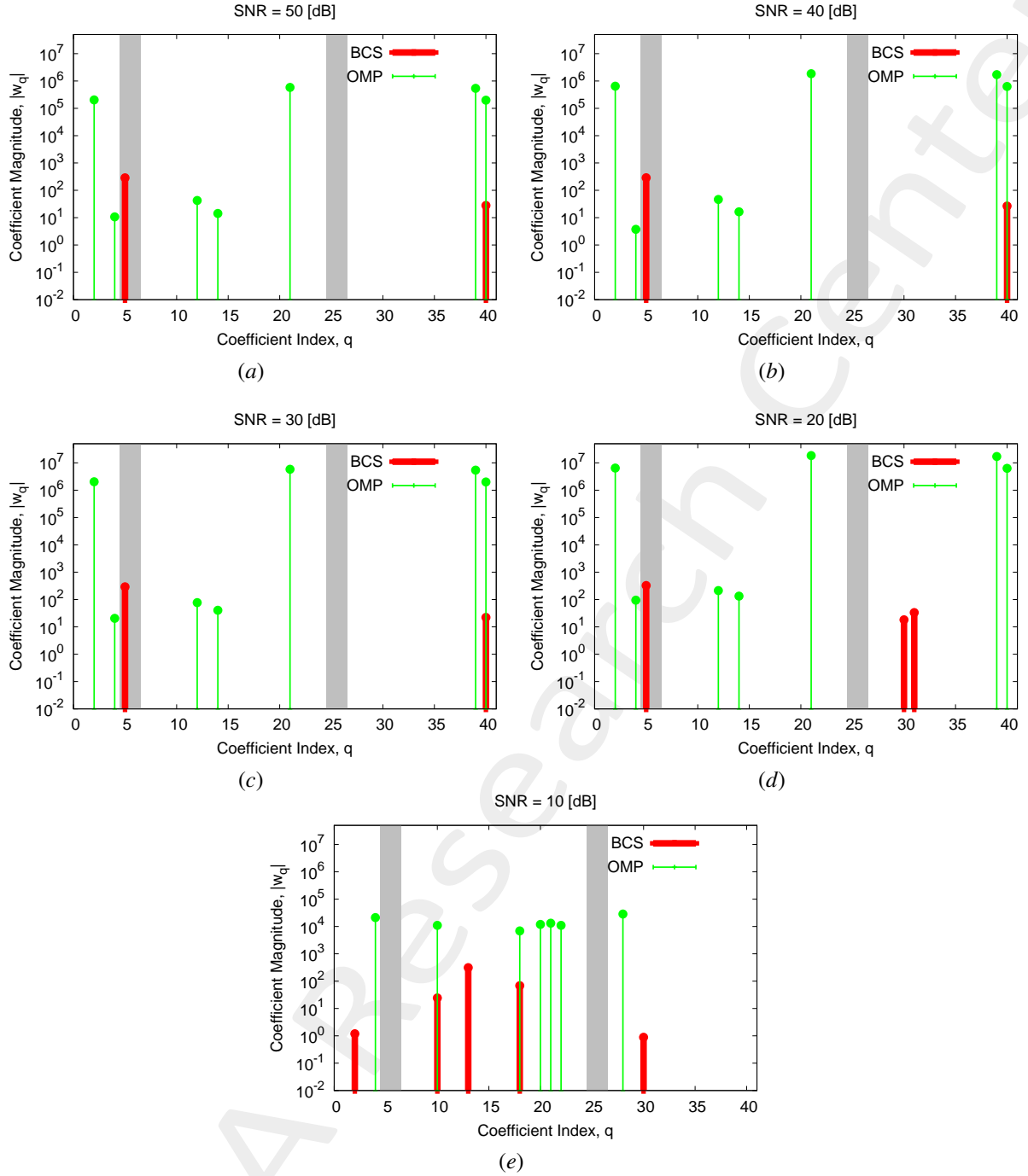
Estimated Coefficients

Figure 11: Coefficient comparison between original (*OMP*) and alternative (*BCS*) MbD : (*a*) $SNR = 50\,[dB]$, (*b*) $SNR = 40\,[dB]$, (*c*) $SNR = 30\,[dB]$, (*d*) $SNR = 20\,[dB]$, (*e*) $SNR = 10\,[dB]$

Observations

The considered *AUT* is characterized by a magnitude failure of an antenna element and a phase failure of another antenna element (i.e., $\nu^{(3)} = 0.45$ and $\gamma^{(3)} = \frac{\pi}{3}\,[rad]$):

- the *OMP* selects vectors related to both magnitude and phase failures but it always fails in identifying the actual failed elements affecting the *AUT* since only vectors not connected to the current failures are chosen.

- the *BCS* algorithm, except for $SNR = 10\,[dB]$, is able to identify the magnitude failure affecting the *AUT* even if

the failure detection is not precise but it does not pick any vector connected to the phase failure affecting the *AUT*.

Computational times

- Δt_{Sim}: Time required to simulate the K *AUT* configurations used to build the $(T \times K)$ "pattern matrix";

- Δt_{SVD}: Time required to perform the *SVD* of the $(T \times K)$ "pattern matrix";

- $\Delta t_{MbE}^{OMP/BCS}$: (Mean) Time required by the Measurement-by-Example tool to read the *SVD* output and perform the estimation of the *AUT* radiated field.

Δt_{Sim} [sec]	4.17×10^4
Δt_{SVD} [sec]	1.53×10^2
Δt_{MbE}^{BCS} [sec]	1.60×10^{-1}
Δt_{MbE}^{OMP} [sec]	8.11×10^{-2}

Table III: Computational times

Remarks

- Given that the number of simulated *AUT*s is $K = S \times (F^{(s)} + P^{(s)}) = 120$, the average per-*AUT* simulation time is

$$\Delta t_{FEKO} \simeq \frac{\Delta t_{Sim}}{K} = \frac{4.17 \times 10^4}{120} \, [sec] = 3.47 \times 10^2 \, [sec]$$

1.2 Different Measurement step $(\Delta_{x/y}^{meas})$ and fixed number of measurement points $M = 25$

The test cases reported in this section are characterized by the following parameters:
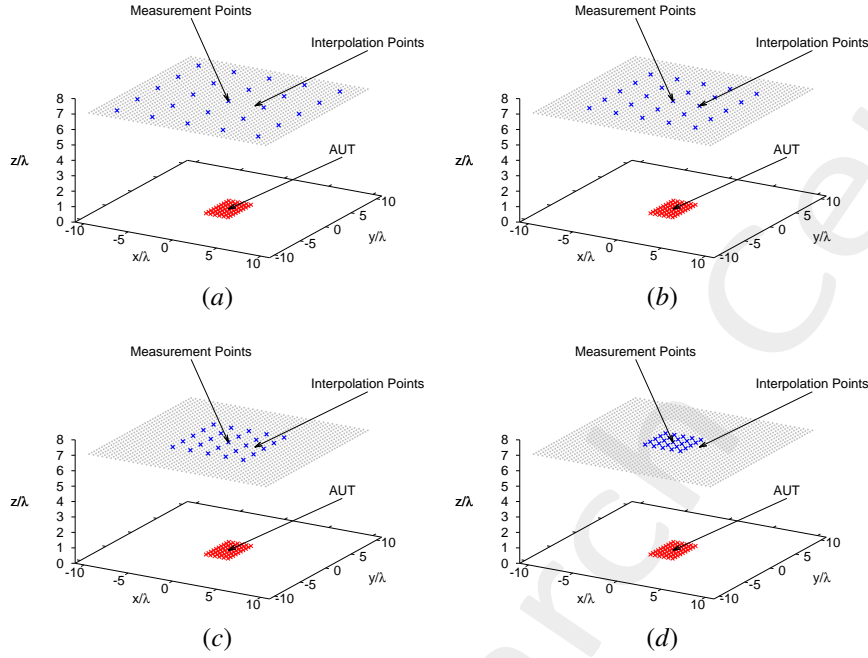
Measurement Set-Up

Figure 12: Disposition of the interpolation points ($T = 1681$) and of the measurement points ($M = 25$) in the near-field region of the *AUT* for considering different measurement plane side dimension : (*a*) $\zeta_{meas} = 16\,[\lambda]$, (*b*)$\zeta_{meas} = 12\,[\lambda]$, (*c*)$\zeta_{meas} = 8\,[\lambda]$, (*d*)$\zeta_{meas} = 4\,[\lambda]$

- Type of measurements : near-field;

- Height of the measurement region : $H = 7\,[\lambda]$;

- Interpolation points :

    - Number of points : $T = 41 \times 41 = 1681$;

    - Length of the interpolation plane side : $\zeta_{x/y}^{int} = \zeta_{int} = 20\,[\lambda]$;

    - Coordinates : $x_t \in [-10, 10]\,[\lambda],\ y_t \in [-10, 10]\,[\lambda],\ z_t = H\,[\lambda],\ t = 1, ..., T$;

    - Interpolation step : $\Delta_{x/y}^{int} = 0.5\,[\lambda]$;

- Measurement points :

    - Number of points : $M_{x/y} = 5 \rightarrow M = 25$;

    - Ratio between number of measurements and total number of elements : $(M/N) = 0.42$;

    - Length of the measurement plane side : $\zeta_{x/y}^{meas} = \zeta_{meas}$ (see Tab. IV)

Plane side, ζ_{meas} [λ]	Points coordinates, $m = 1, ..., M$			Measurement step, $\Delta_{x/y}^{meas}$ [λ]
	x_m^{meas} [λ]	y_m^{meas} [λ]	z_m^{meas} [λ]	
16	$[-8, 8]$	$[-8, 8]$	7	4
12	$[-6, 6]$	$[-6, 6]$	7	3
8	$[-4, 4]$	$[-4, 4]$	7	2
4	$[-2, 2]$	$[-2, 2]$	7	1

Table IV: Table of parameters considered for the different test cases analyzed

1.2.1 Plane dimension side : $\zeta_{meas} = 16\,[\lambda]$

Original (*OMP*) MbD parameters

- Max. number of iterations of the OMP algorithm : $I = \{1;\ 2;\ 3;\ ...;\ 20\}$;

- Selected iteration to report the results: $I = 3$; this choice is justified by the fact that at this iteration the *OMP* algorithm reaches the best near field error as shown in the following Fig. 13.
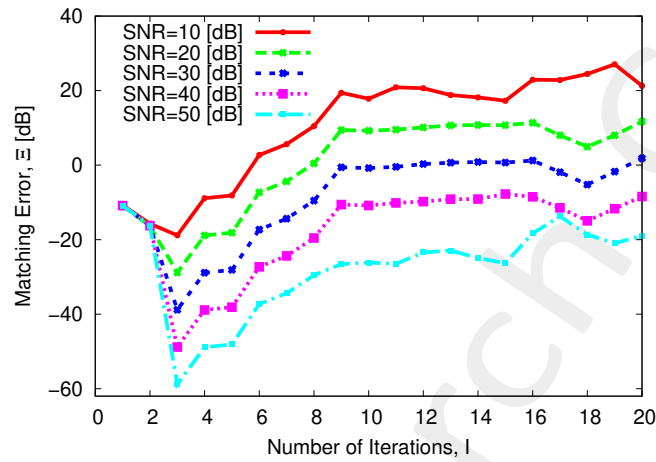

Figure 13: Behaviour of the near-field matching error versus the number of *OMP* iterations, I.

Evaluation of the Truncation Error from Actual Near-Field Data

In order to evaluate the truncation error, in the following figure is predented a visual comparison of the near-field radiated by the *AUT* measured over the full interpolation plane (ζ_{int}) and on the truncated region (ζ_{meas}), as well as the corresponding far-field patterns obtained with NF-FF transformation. The truncated near-field has been obtained as follows:

$$ E_{tr}(x,y) = \begin{cases} E(x,y) & if \quad -\frac{\zeta_{meas}}{2} \leq \tau \leq \frac{\zeta_{meas}}{2} \\ 0 & otherwise \end{cases} \quad ; \; -\frac{\zeta_{int}}{2} \leq \tau \leq \frac{\zeta_{int}}{2} $$
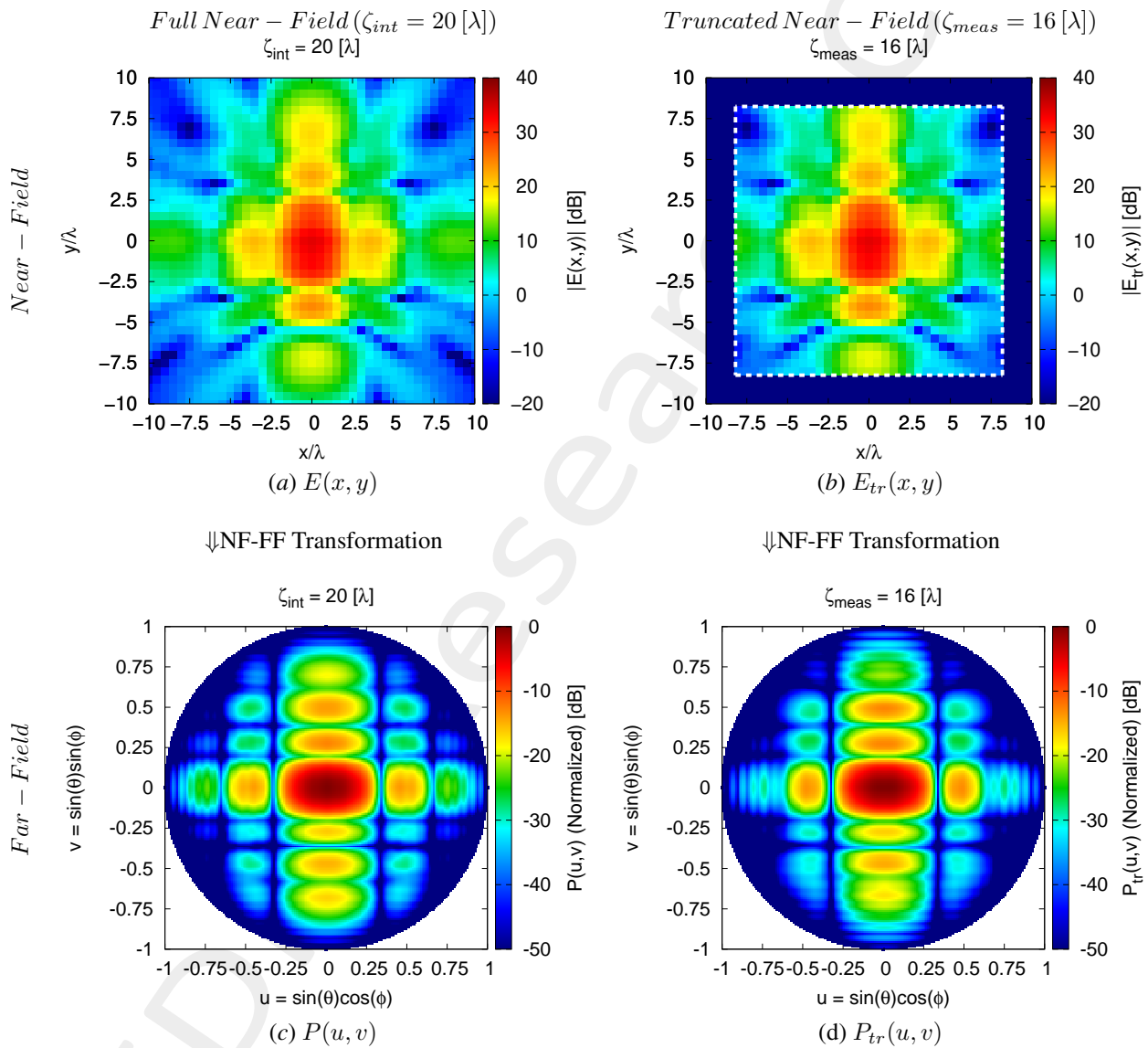
where $\tau = x,\,y$.

Figure 14: $\zeta_{meas} = 16\,[\lambda]$ - (*a*)(*b*) Near-field and (*c*)(*d*) far-field patterns obtained via NF-FF transformation for the actual *AUT*.

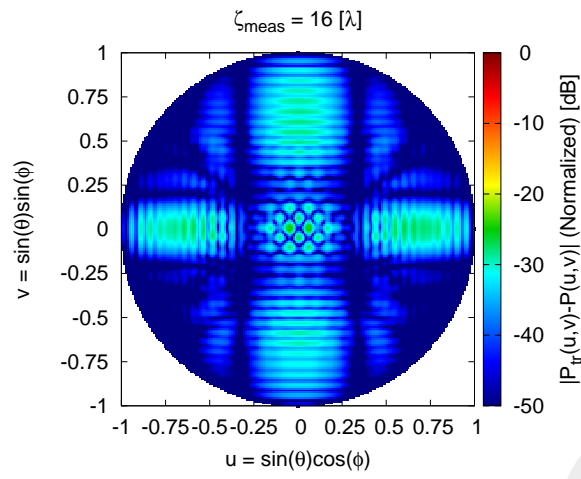Figure 15: $\zeta_{meas} = 16\,[\lambda]$ - Difference between the full and the truncated far-fields, $|P(u,v) - P_{tr}(u,v)|$.

Near-Field Error

The comparison, in terms of near field error, between the original (*OMP*) and the alternative (*BCS*) MbD is reported in the following Fig. 16:
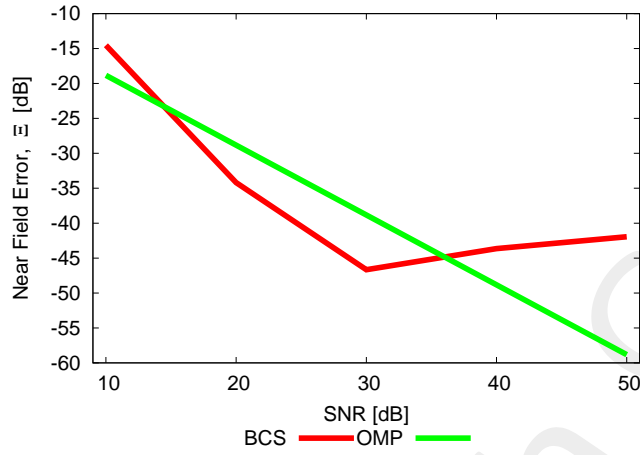

Figure 16: Near Field Error comparison between original (*OMP*) and alternative (*BCS*) MbD for different SNR values

$SNR\,[dB]$	$Near\ Field\ Error,\ \Xi\ [dB]$	
	BCS	OMP
50	-41.95	-58.83
40	-43.64	-48.83
30	-46.66	-38.83
20	-34.19	-28.83
10	-14.53	-18.83

Table V: Near Field Errors obtained by the original (*OMP*) and alternative (*BCS*) MbD

Observations

- the *OMP* error decreases linearly with the increase of the SNR value obtaining a near-field error $\Xi < -25\,[dB]$ already from $SNR = 20\,[dB]$. Moreover, for $SNR \geq 35\,[dB]$, this solver substantially outperforms the other one;

- the *BCS* reaches the lowest error for the range $15\,[dB] \leq SNR \leq 35\,[dB]$ but for higher SNR values it loses the comparison with the *OMP* because the *BCS* error does not decrease with the increase of the SNR value.

Estimated Near-Field

(a) *Magnitude* — AUT

(b) *Phase* — AUT

$|\mathbf{E}_{\mathbf{AUT}} - \tilde{\mathbf{E}}_{\mathbf{AUT}}|$

OMP   BCS

$SNR = 50\,[dB]$ — (c), (d)

$SNR = 40\,[dB]$ — (e), (f)

$SNR = 30\,[dB]$ — (g), (h)

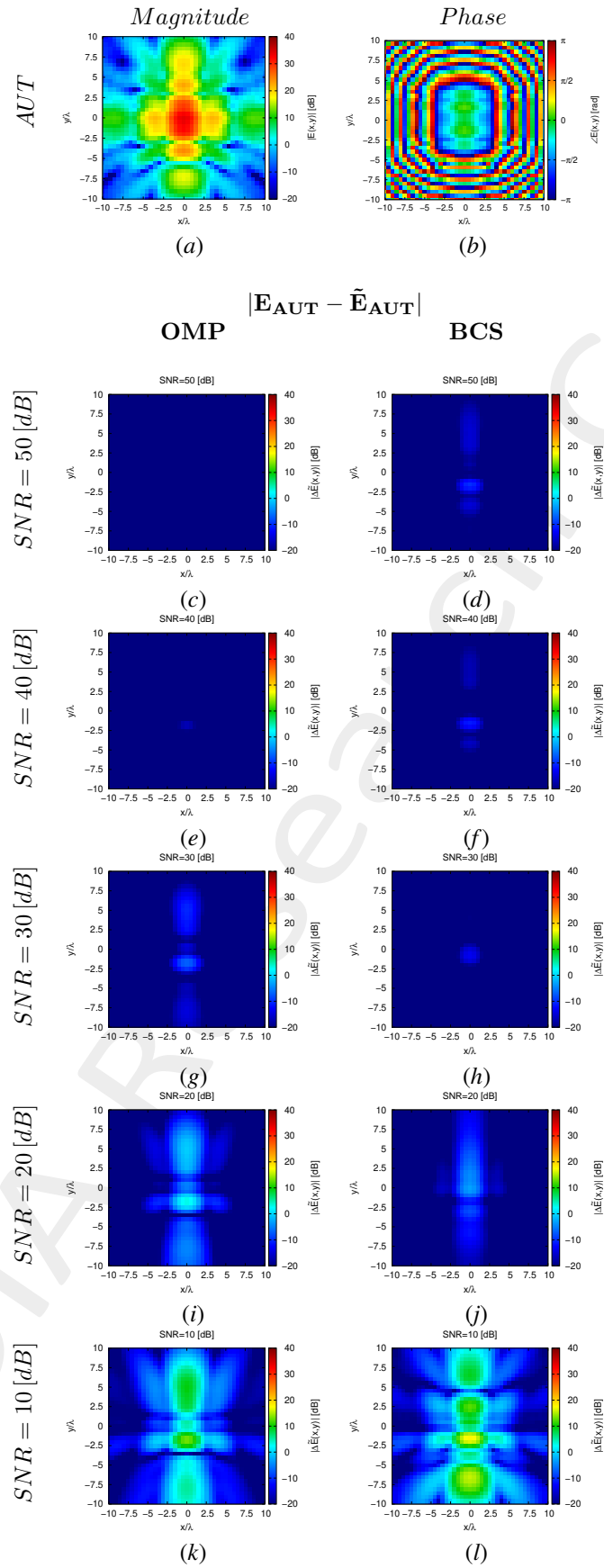$SNR = 20\,[dB]$ — (i), (j)

$SNR = 10\,[dB]$ — (k), (l)

Figure 17: Magnitude difference between the actual and estimated $2-D$ near-field pattern when processing noisy measurements at different SNRs.
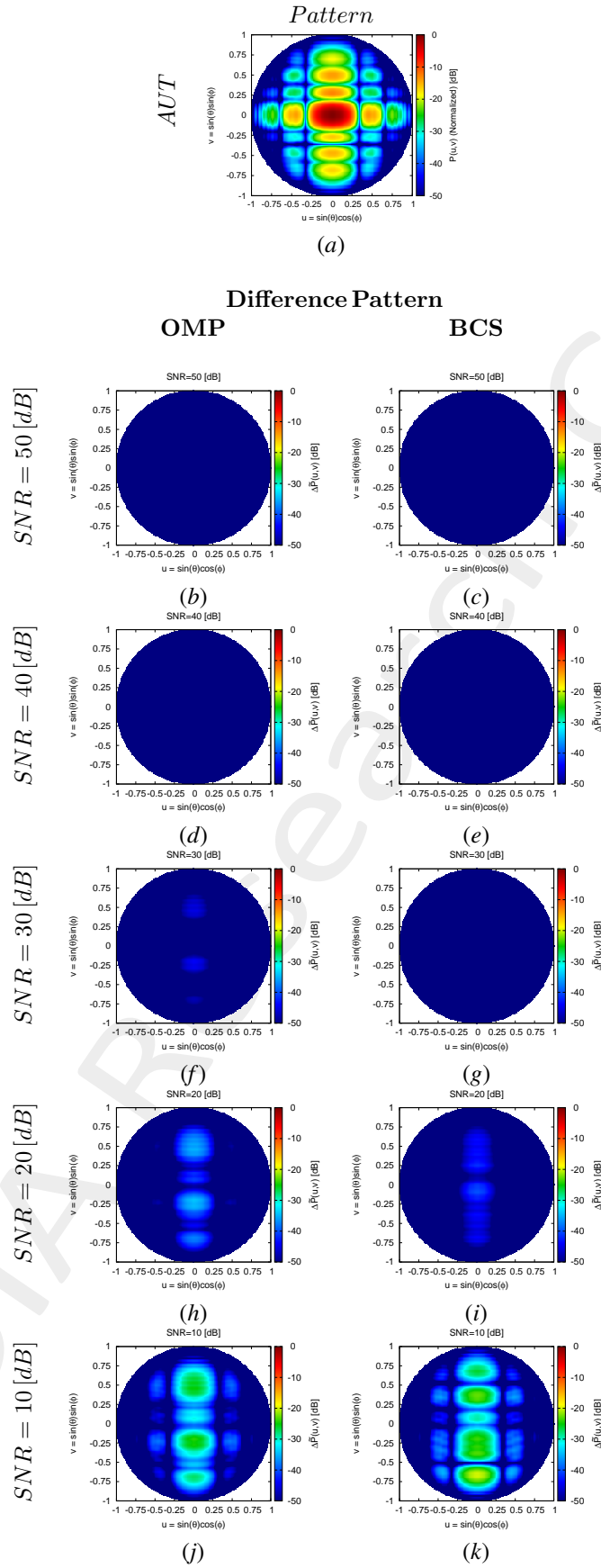
Estimated Far-Field

Figure 18: Difference between the actual and estimated $2 - D$ far-field pattern when processing noisy measurements at different SNRs.

Figure 19: $1 - D$ cuts of the estimated far-field pattern (obtained through near-to-far-field transformation from the estimated near-field patterns) under several noisy conditions
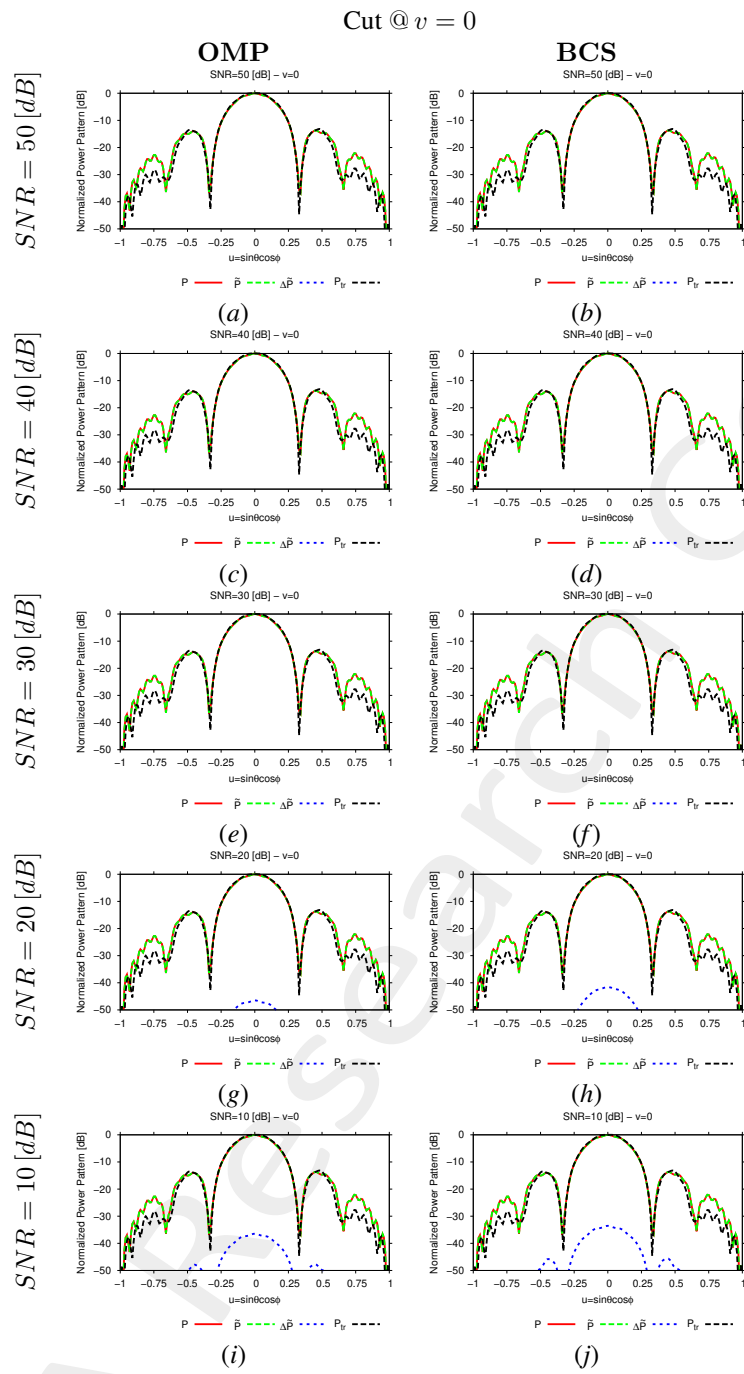
Cut @ $u = 0$

Figure 20: $1 - D$ cuts of the estimated far-field pattern (obtained through near-to-far-field transformation from the estimated near-field patterns) under several noisy conditions
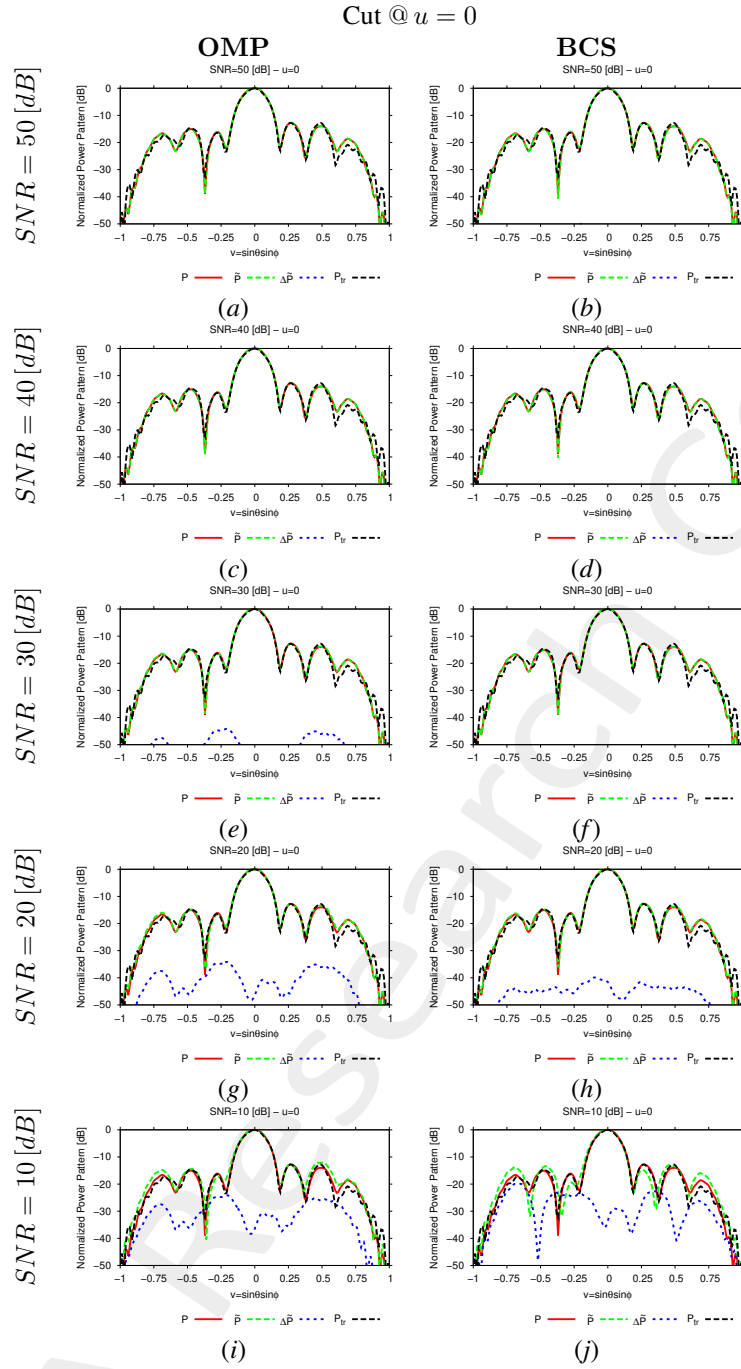
$SNR\,[dB]$	$Far - Field\ Error,\ \chi\ [dB]$	
	BCS	OMP
50	-43.13	-59.86
40	-45.01	-49.86
30	-48.36	-39.86
20	-34.85	-29.86
10	-16.49	-19.85

Table VI: Far-field matching error between the actual and estimated AUT patterns (both obtained through near-to-far-field transformation from the corresponding near-field patterns) under several noisy conditions.
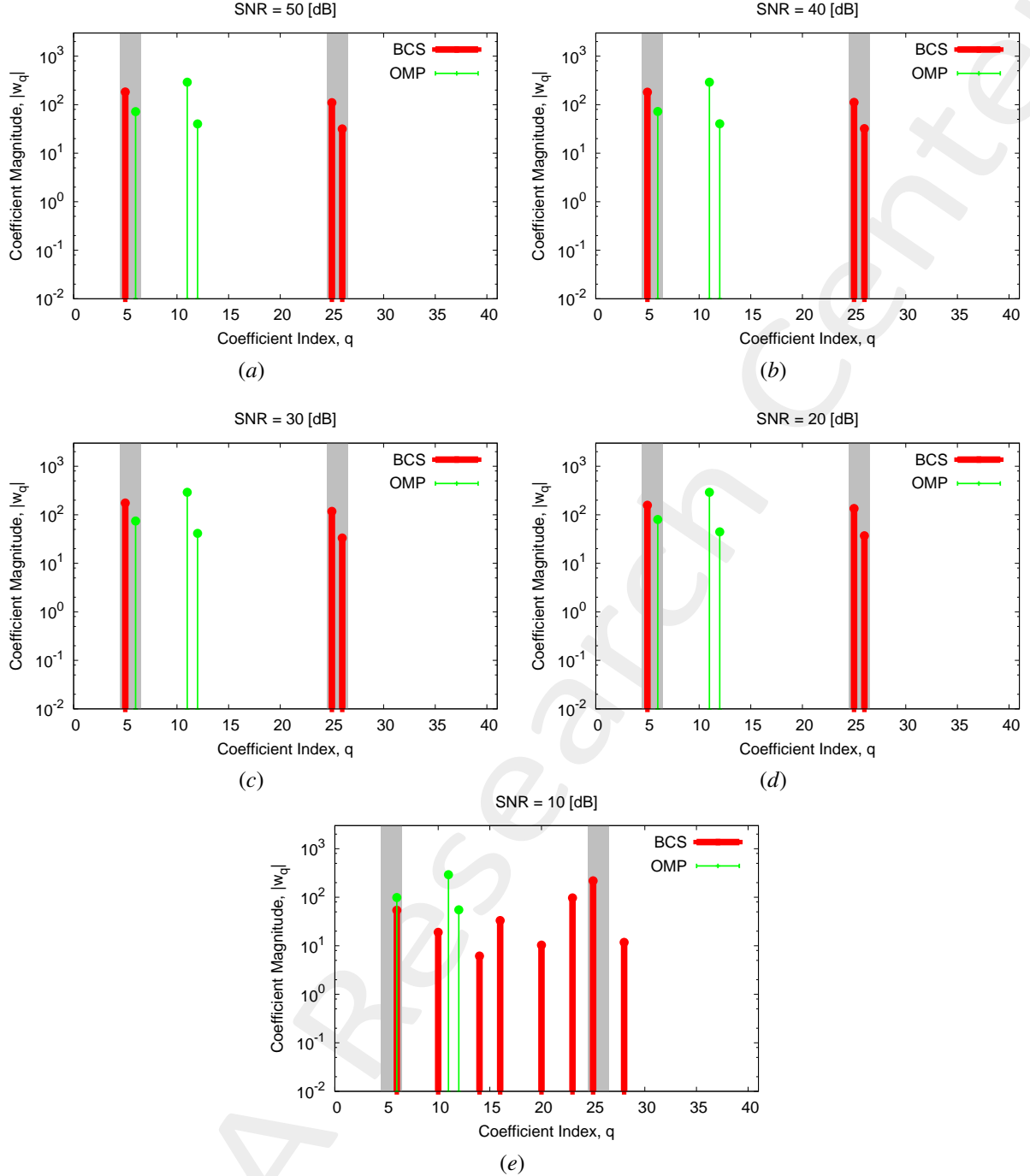
Estimated Coefficients

Figure 21: Coefficient comparison between original (*OMP*) and alternative (*BCS*) MbD : (*a*) $SNR = 50\,[dB]$, (*b*) $SNR = 40\,[dB]$, (*c*) $SNR = 30\,[dB]$, (*d*) $SNR = 20\,[dB]$, (*e*) $SNR = 10\,[dB]$

Observations

The considered *AUT* is characterized by a magnitude failure of an antenna element and a phase failure of another antenna element (i.e., $\nu^{(3)} = 0.45$ and $\gamma^{(3)} = \frac{\pi}{3}\,[rad]$):

- the *OMP* always selects the same three vectors which are related only to magnitude failures. Moreover, for the entire SNR range, this algorithm is able to correctly detect the magnitude failure even if the detection is not precise since other vectors not connected to the current failure are chosen. The *OMP* fails in detecting the phase failure affecting the *AUT* because none of the vectors related to the actual phase failure has been selected.

- the *BCS* algorithm is able to precisely identify both the failures affecting the AUT already from $SNR = 20\,[dB]$. Instead, at $SNR = 10\,[dB]$, the BCS is still able to find the both failures but this detection is not precise since the method selects also vectors not connected to the actual failures.

Computational times

- Δt_{Sim}: Time required to simulate the K *AUT* configurations used to build the $(T \times K)$ "pattern matrix";

- Δt_{SVD}: Time required to perform the *SVD* of the $(T \times K)$ "pattern matrix";

- $\Delta t_{MbE}^{OMP/BCS}$: (Mean) Time required by the Measurement-by-Example tool to read the *SVD* output and perform the estimation of the *AUT* radiated field.

$\Delta t_{Sim}\ [sec]$	4.17×10^4
$\Delta t_{SVD}\ [sec]$	1.53×10^2
$\Delta t_{MbE}^{BCS}\ [sec]$	1.71×10^{-1}
$\Delta t_{MbE}^{OMP}\ [sec]$	8.39×10^{-2}

Table VII: Computational times

Remarks

- Given that the number of simulated *AUT*s is $K = S \times (F^{(s)} + P^{(s)}) = 120$, the average per-*AUT* simulation time is

$$\Delta t_{FEKO} \simeq \frac{\Delta t_{Sim}}{K} = \frac{4.17 \times 10^4}{120}\,[sec] = 3.47 \times 10^2\,[sec]$$

1.2.2 Plane dimension side : $\zeta_{meas} = 12\,[\lambda]$

Original (*OMP*) MbD parameters

- Max. number of iterations of the OMP algorithm : $I = \{1; 2; 3; ...; 20\}$;

- Selected iteration to report the results: $I = 14$; this choice is justified by the fact that at this iteration the *OMP* algorithm reaches the best near field error as shown in the following Fig. 22.
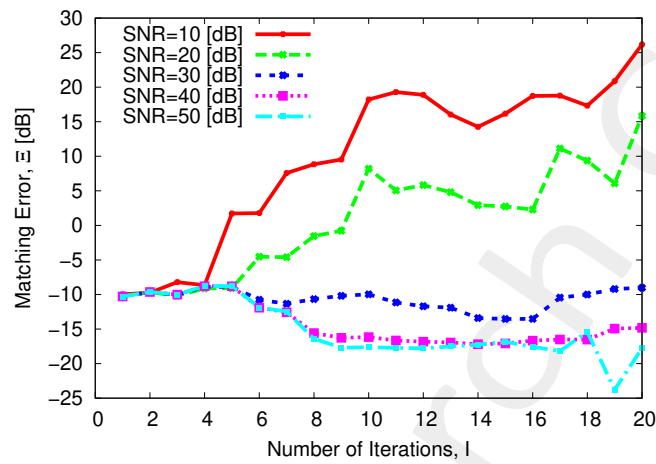

Figure 22: Behaviour of the near-field matching error versus the number of *OMP* iterations, I.

Evaluation of the Truncation Error from Actual Near-Field Data

In order to evaluate the truncation error, in the following figure is predented a visual comparison of the near-field radiated by the *AUT* measured over the full interpolation plane (ζ_{int}) and on the truncated region (ζ_{meas}), as well as the corresponding far-field patterns obtained with NF-FF transformation. The truncated near-field has been obtained as follows:

$$E_{tr}(x,y) = \begin{cases} E(x,y) & if \quad -\frac{\zeta_{meas}}{2} \leq \tau \leq \frac{\zeta_{meas}}{2} \\ 0 & otherwise \end{cases} \quad ; -\frac{\zeta_{int}}{2} \leq \tau \leq \frac{\zeta_{int}}{2}$$
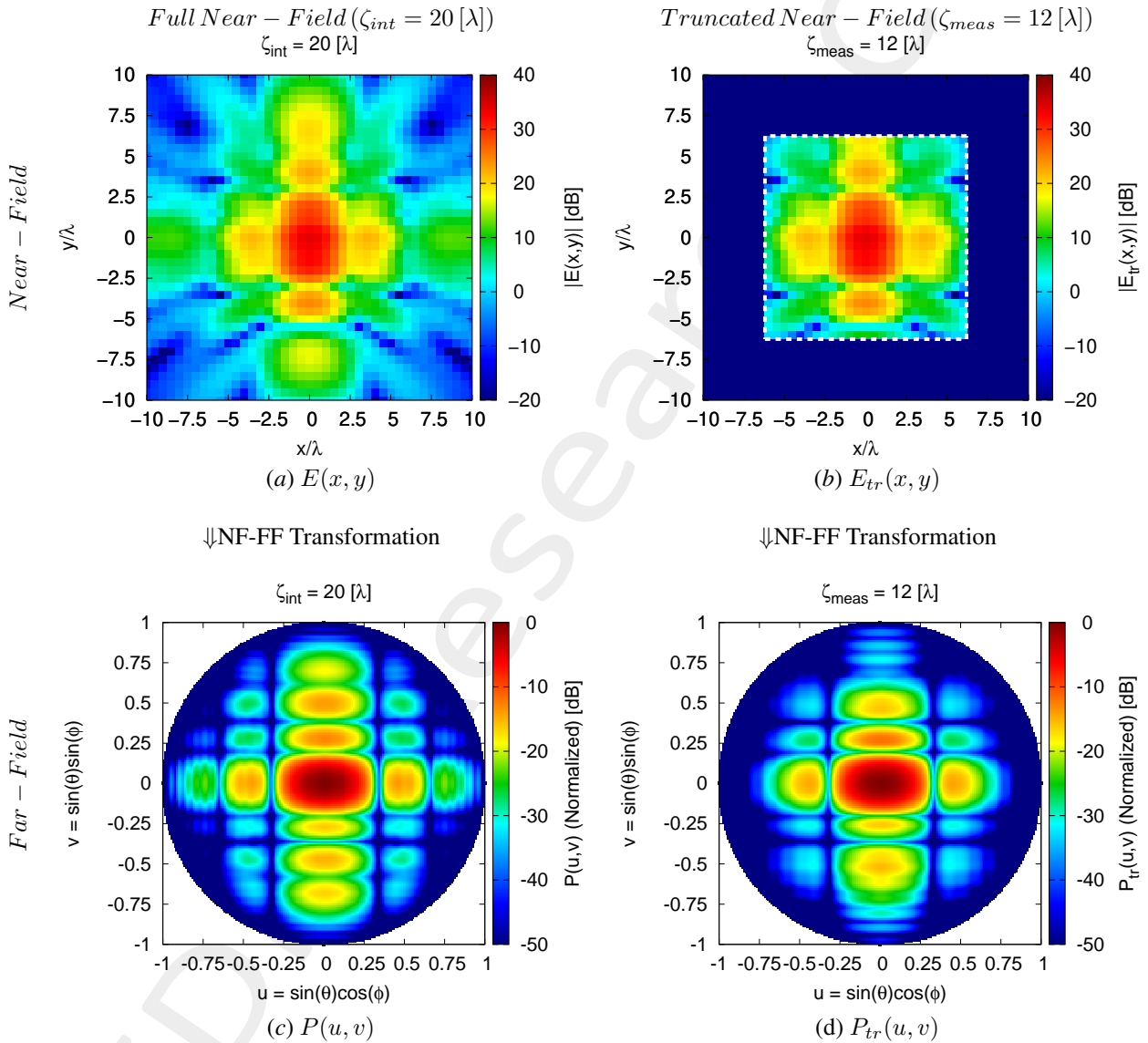
where $\tau = x, y$.

Figure 23: $\zeta_{meas} = 12\,[\lambda]$ - (*a*)(*b*) Near-field and (*c*)(*d*) far-field patterns obtained via NF-FF transformation for the actual *AUT*.

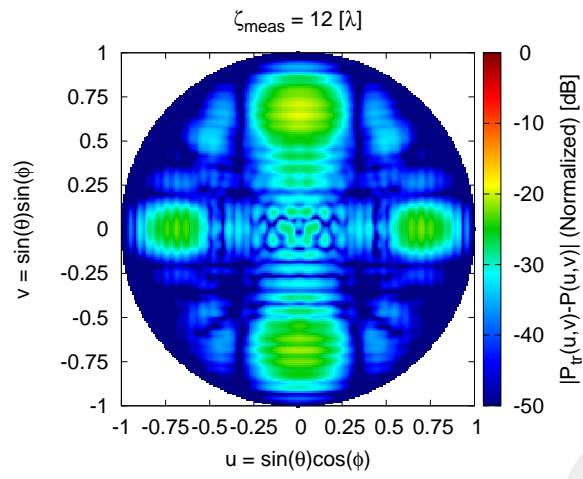Figure 24: $\zeta_{meas} = 12\,[\lambda]$ - Difference between the full and the truncated far-fields, $|P(u,v) - P_{tr}(u,v)|$.

Near-Field Error

The comparison, in terms of near field error, between the original (*OMP*) and the alternative (*BCS*) MbD is reported in the following Fig. 25:
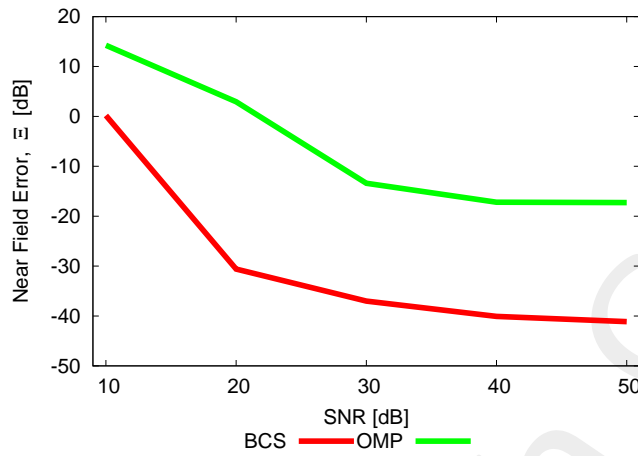

Figure 25: Near Field Error comparison between original (*OMP*) and alternative (*BCS*) MbD for different SNR values

$SNR\,[dB]$	$Near\ Field\ Error,\ \Xi\ [dB]$	
	BCS	OMP
50	-41.14	-17.27
40	-40.09	-17.19
30	-37.01	-13.41
20	-30.59	2.93
10	0.19	14.25

Table VIII: Near Field Errors obtained by the original (*OMP*) and alternative (*BCS*) MbD

Observations

- the *OMP* performs poorly since even at high SNR values the achieved near-field error does not go below $-18\,[dB]$ meaning that the near-field reconstruction is not accurate;

- the *BCS* algorithm obtains an error $\Xi < -30\,[dB]$ for $SNR \geq 20\,[dB]$; in particular, the error highly decreases in the range $10\,[dB] \leq SNR \leq 20\,[dB]$ but then the decrease reduces as the SNR increases as proved by the variation of only $1\,[dB]$ from the error at $SNR = 40\,[dB]$ to that at $SNR = 50\,[dB]$.

Estimated Near-Field
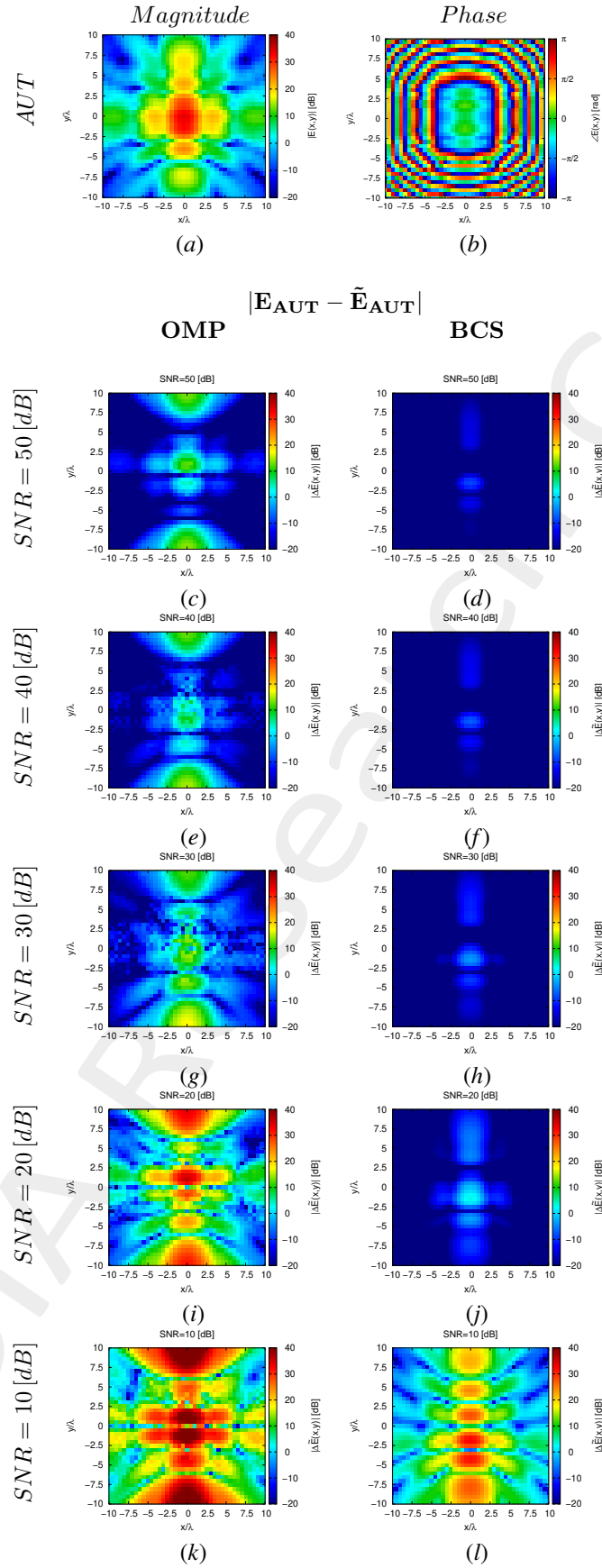

Figure 26: Magnitude difference between the actual and estimated $2 - D$ near-field pattern when processing noisy measurements at different SNRs.

Estimated Far-Field

(a)

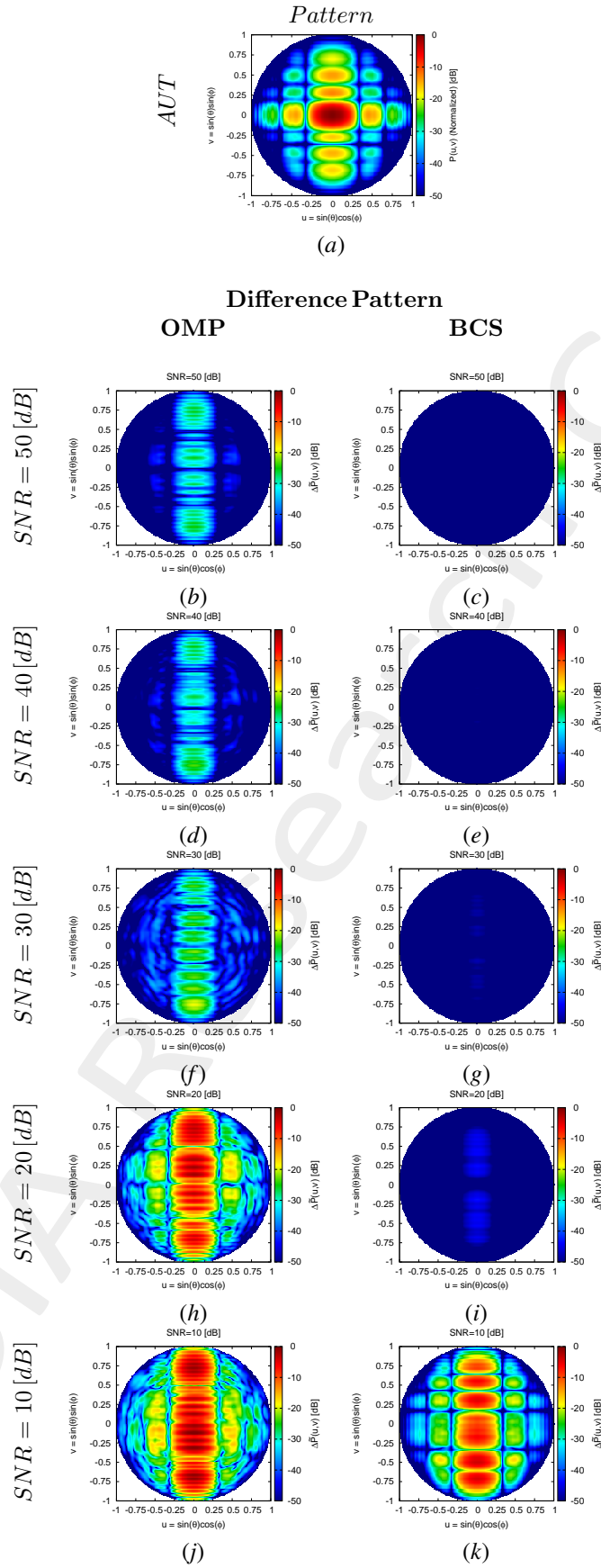**Difference Pattern**

OMP   BCS

Figure 27: Difference between the actual and estimated $2-D$ far-field pattern when processing noisy measurements at different SNRs.

Cut @ $v = 0$

Figure 28: $1 - D$ cuts of the estimated far-field pattern (obtained through near-to-far-field transformation from the estimated near-field patterns) under several noisy conditions
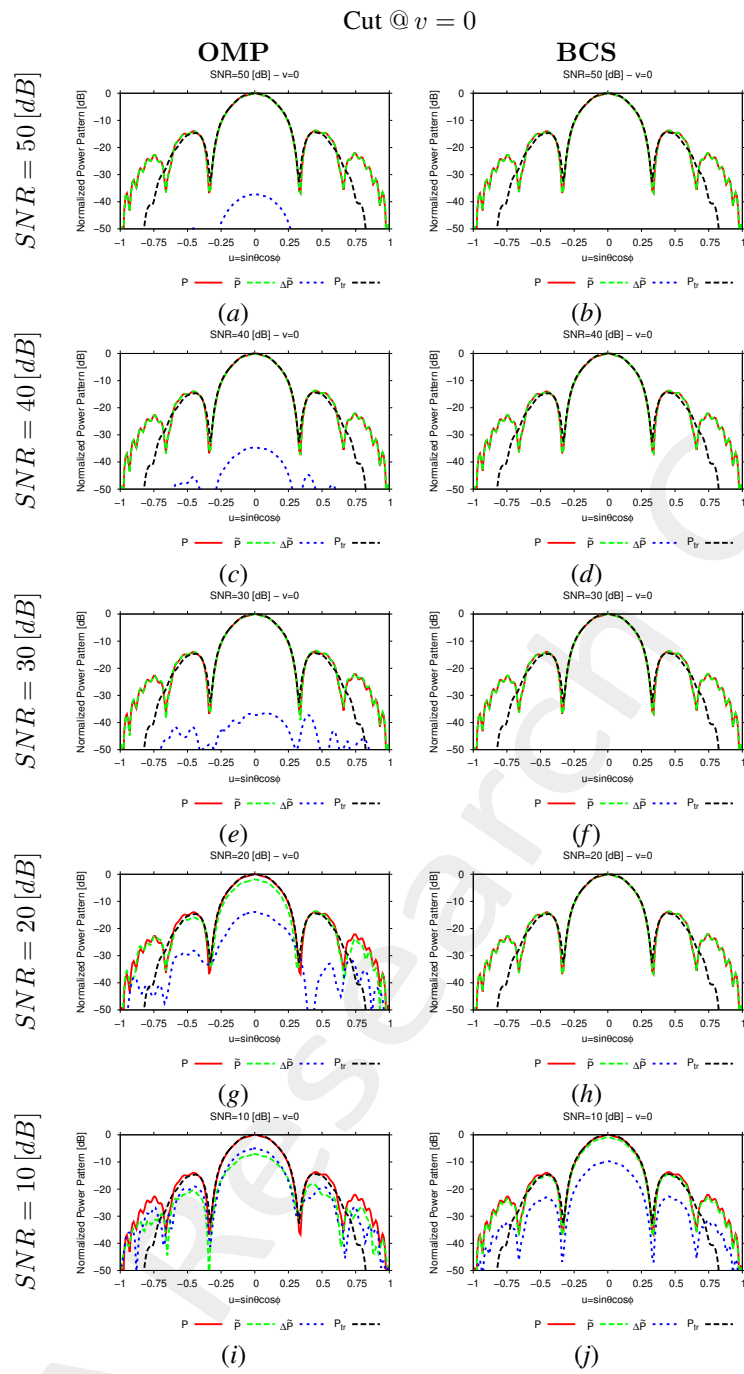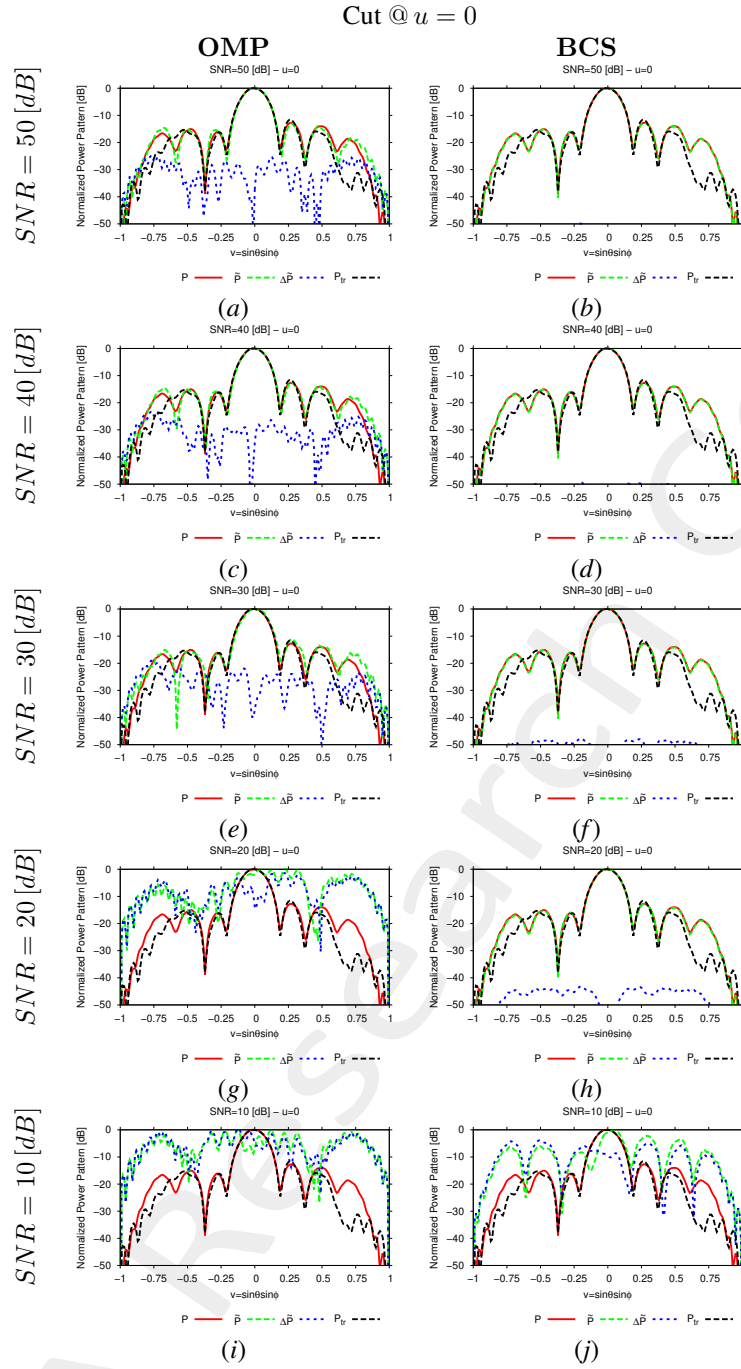
Figure 29: $1 - D$ cuts of the estimated far-field pattern (obtained through near-to-far-field transformation from the estimated near-field patterns) under several noisy conditions

$SNR\,[dB]$	$Far - Field\ Error,\ \chi\ [dB]$	
	BCS	OMP
50	-43.03	-20.52
40	-42.52	-20.12
30	-40.87	-16.00
20	-36.44	2.76
10	0.94	4.79

Table IX: Far-field matching error between the actual and estimated AUT patterns (both obtained through near-to-far-field transformation from the corresponding near-field patterns) under several noisy conditions.
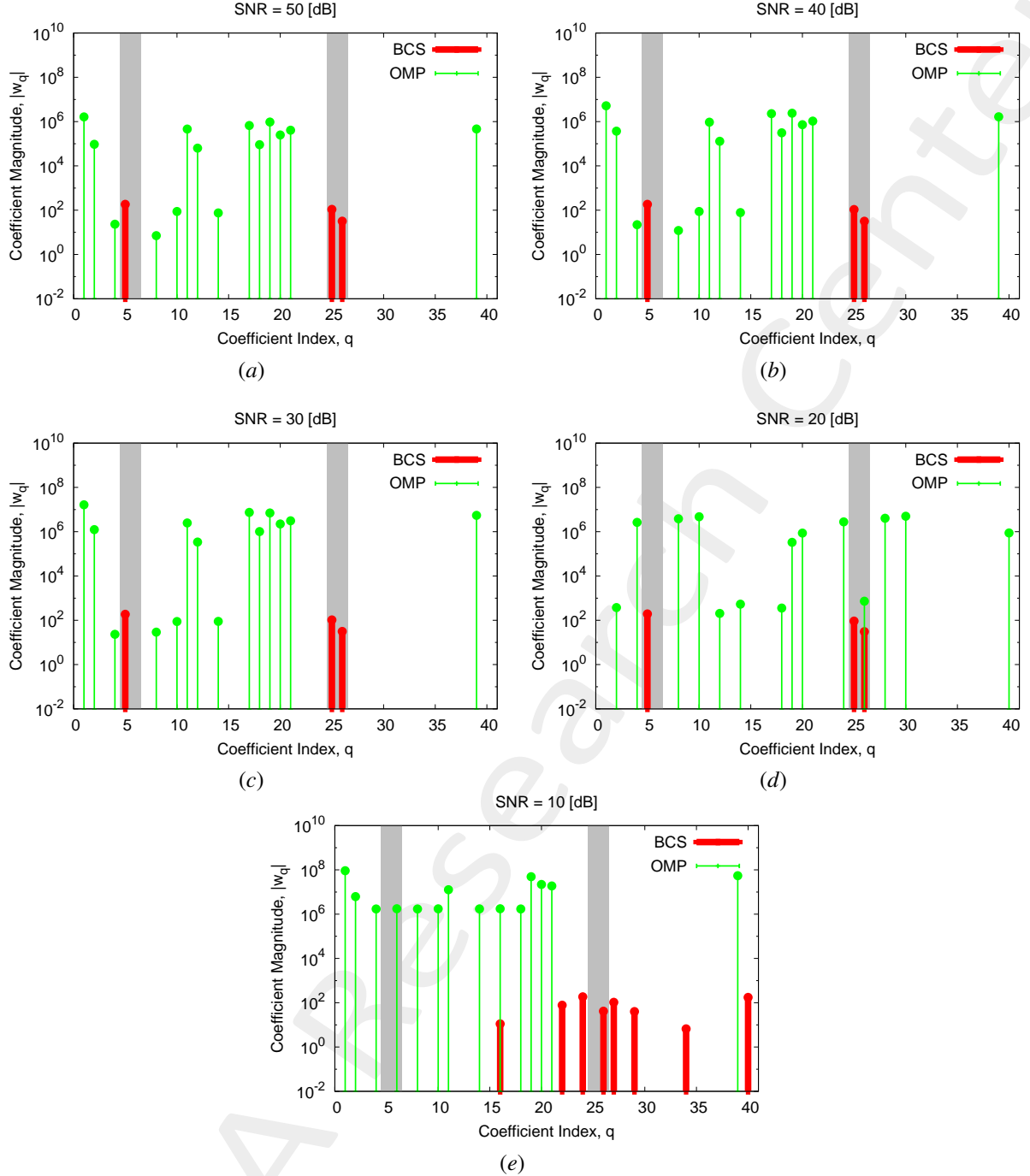
Estimated Coefficients

Figure 30: Coefficient comparison between original (*OMP*) and alternative (*BCS*) MbD : (*a*) $SNR = 50 \, [dB]$, (*b*) $SNR = 40 \, [dB]$, (*c*) $SNR = 30 \, [dB]$, (*d*) $SNR = 20 \, [dB]$, (*e*) $SNR = 10 \, [dB]$

Observations

The considered *AUT* is characterized by a magnitude failure of an antenna element and a phase failure of another antenna element (i.e., $\nu^{(3)} = 0.45$ and $\gamma^{(3)} = \frac{\pi}{3} \, [rad]$):

- the *OMP* selects vectors related to both magnitude and phase failures but it fails in identifying the actual failed elements affecting the *AUT* except at $SNR = 20 \, [dB]$, where the phase failure is identified, and at $SNR = 10 \, [dB]$, where the magnitude failure is detected. However, the mentioned detections can be considered just fortuitous events since they are not confirmed at other SNR values;

- the *BCS* algorithm is able to precisely identify both the failures affecting the AUT already starting from $SNR = 20\,[dB]$.

Computational times

- Δt_{Sim}: Time required to simulate the K *AUT* configurations used to build the $(T \times K)$ "pattern matrix";

- Δt_{SVD}: Time required to perform the *SVD* of the $(T \times K)$ "pattern matrix";

- $\Delta t_{MbE}^{OMP/BCS}$: (Mean) Time required by the Measurement-by-Example tool to read the *SVD* output and perform the estimation of the *AUT* radiated field.

$\Delta t_{Sim}\ [sec]$	4.17×10^4
$\Delta t_{SVD}\ [sec]$	1.53×10^2
$\Delta t_{MbE}^{BCS}\ [sec]$	1.38×10^{-1}
$\Delta t_{MbE}^{OMP}\ [sec]$	8.51×10^{-2}

Table X: Computational times

Remarks

- Given that the number of simulated *AUT*s is $K = S \times (F^{(s)} + P^{(s)}) = 120$, the average per-*AUT* simulation time is

$$\Delta t_{FEKO} \simeq \frac{\Delta t_{Sim}}{K} = \frac{4.17 \times 10^4}{120}\,[sec] = 3.47 \times 10^2\,[sec]$$

More information on the topics of this document can be found in the following list of references.

References

[1] M. Salucci, N. Anselmi, M. D. Migliore and A. Massa, "A bayesian compressive sensing approach to robust near-field antenna characterization," *IEEE Trans. Antennas Propag.*, vol. 70, no. 9, pp. 8671-8676, Sep. 2022 (DOI: 10.1109/TAP.2022.3177528).

[2] B. Li, M. Salucci, W. Tang, and P. Rocca, "Reliable field strength prediction through an adaptive total-variation CS technique," *IEEE Antennas Wirel. Propag. Lett.*, vol. 19, no. 9, pp. 1566-1570, Sep. 2020.

[3] M. Salucci, M. D. Migliore, P. Rocca, A. Polo, and A. Massa, "Reliable antenna measurements in a near-field cylindrical setup with a sparsity promoting approach," *IEEE Trans. Antennas Propag.*, vol. 68, no. 5, pp. 4143-4148, May 2020.

[4] G. Oliveri, M. Salucci, N. Anselmi, and A. Massa, "Compressive sensing as applied to inverse problems for imaging: theory, applications, current trends, and open challenges," *IEEE Antennas Propag. Mag. - Special Issue on "Electromagnetic Inverse Problems for Sensing and Imaging,"* vol. 59, no. 5, pp. 34-46, Oct. 2017.

[5] A. Massa, P. Rocca, and G. Oliveri, "Compressive sensing in electromagnetics - A review," *IEEE Antennas Propag. Mag.*, pp. 224-238, vol. 57, no. 1, Feb. 2015.

[6] A. Massa and F. Texeira, "Guest-Editorial: Special Cluster on Compressive Sensing as Applied to Electromagnetics," *IEEE Antennas Wirel. Propag. Lett.*, vol. 14, pp. 1022-1026, 2015.

[7] G. Oliveri, N. Anselmi, M. Salucci, L. Poli, and A. Massa, "Compressive sampling-based scattering data acquisition in microwave imaging," *J. Electromagn. Waves Appl*, vol. 37, no. 5, 693-729, March 2023 (DOI: 10.1080/09205071.2023.2188263).

[8] G. Oliveri, L. Poli, N. Anselmi, M. Salucci, and A. Massa, "Compressive sensing-based Born iterative method for tomographic imaging," *IEEE Trans. Microw. Theory Techn.*, vol. 67, no. 5, pp. 1753-1765, May 2019.

[9] M. Salucci, L. Poli, and G. Oliveri, "Full-vectorial 3D microwave imaging of sparse scatterers through a multi-task Bayesian compressive sensing approach," *J. Imaging*, vol. 5, no. 1, pp. 1-24, Jan. 2019.

[10] M. Salucci, A. Gelmini, L. Poli, G. Oliveri, and A. Massa, "Progressive compressive sensing for exploiting frequency-diversity in GPR imaging," *J. Electromagn. Waves Appl.*, vol. 32, no. 9, pp. 1164-1193, 2018.

[11] N. Anselmi, L. Poli, G. Oliveri, and A. Massa, "Iterative multi-resolution bayesian CS for microwave imaging," *IEEE Trans. Antennas Propag.*, vol. 66, no. 7, pp. 3665-3677, Jul. 2018.

[12] N. Anselmi, G. Oliveri, M. A. Hannan, M. Salucci, and A. Massa, "Color compressive sensing imaging of arbitrary-shaped scatterers," *IEEE Trans. Microw. Theory Techn.*, vol. 65, no. 6, pp. 1986-1999, Jun. 2017.

[13] N. Anselmi, G. Oliveri, M. Salucci, and A. Massa, "Wavelet-based compressive imaging of sparse targets" *IEEE Trans. Antennas Propag.*, vol. 63, no. 11, pp. 4889-4900, Nov. 2015.

[14] G. Oliveri, P.-P. Ding, and L. Poli, "3D crack detection in anisotropic layered media through a sparseness-regularized solver," *IEEE Antennas Wirel. Propag. Lett.*, vol. 14, pp. 1031-1034, 2015.

[15] L. Poli, G. Oliveri, P.-P. Ding, T. Moriyama, and A. Massa, "Multifrequency Bayesian compressive sensing methods for microwave imaging," *J. Opt. Soc. Am. A*, vol. 31, no. 11, pp. 2415-2428, 2014.

[16] G. Oliveri, N. Anselmi, and A. Massa, "Compressive sensing imaging of non-sparse 2D scatterers by a total-variation approach within the Born approximation," *IEEE Trans. Antennas Propag.*, vol. 62, no. 10, pp. 5157-5170, Oct. 2014.

[17] L. Poli, G. Oliveri, F. Viani, and A. Massa, "MT-BCS-based microwave imaging approach through minimum-norm current expansion," *IEEE Trans. Antennas Propag.*, vol. 61, no. 9, pp. 4722-4732, Sep. 2013.

[18] F. Viani, L. Poli, G. Oliveri, F. Robol, and A. Massa, "Sparse scatterers imaging through approximated multitask compressive sensing strategies," *Microwave Opt. Technol. Lett.*, vol. 55, no. 7, pp. 1553-1558, Jul. 2013.

[19] L. Poli, G. Oliveri, P. Rocca, and A. Massa, "Bayesian compressive sensing approaches for the reconstruction of two-dimensional sparse scatterers under TE illumination," *IEEE Trans. Geosci. Remote Sensing*, vol. 51, no. 5, pp. 2920-2936, May 2013.

[20] P. Rocca, N. Anselmi, M. A. Hannan, and A. Massa, "Conical frustum multi-beam phased arrays for air traffic control radars," *Sensors*, vol. 22, no. 19, 7309, pp. 1-18, 2022 (DOI: 10.3390/s22197309)

[21] F. Zardi, G. Oliveri, M. Salucci, and A. Massa, "Minimum-complexity failure correction in linear arrays via compressive processing," *IEEE Trans. Antennas Propag.*, vol. 69, no. 8, pp. 4504-4516, Aug. 2021.

[22] N. Anselmi, G. Gottardi, G. Oliveri, and A. Massa, "A total-variation sparseness-promoting method for the synthesis of contiguously clustered linear architectures," *IEEE Trans. Antennas Propag.*, vol. 67, no. 7, pp. 4589-4601, Jul. 2019.

[23] M. Salucci, A. Gelmini, G. Oliveri, and A. Massa, "Planar arrays diagnosis by means of an advanced Bayesian compressive processing," *IEEE Trans. Antennas Propag.*, vol. 66, no. 11, pp. 5892-5906, Nov. 2018.

[24] L. Poli, G. Oliveri, P. Rocca, M. Salucci, and A. Massa, "Long-Distance WPT Unconventional Arrays Synthesis," *J. Electromagn. Waves Appl.*, vol. 31, no. 14, pp. 1399-1420, Jul. 2017.

[25] G. Oliveri, M. Salucci, and A. Massa, "Synthesis of modular contiguously clustered linear arrays through a sparseness-regularized solver," *IEEE Trans. Antennas Propag.*, vol. 64, no. 10, pp. 4277-4287, Oct. 2016.

[26] M. Carlin, G. Oliveri, and A. Massa, "Hybrid BCS-deterministic approach for sparse concentric ring isophoric arrays," *IEEE Trans. Antennas Propag.*, vol. 63, no. 1, pp. 378-383, Jan. 2015.

[27] G. Oliveri, E. T. Bekele, F. Robol, and A. Massa, "Sparsening conformal arrays through a versatile BCS-based method," *IEEE Trans. Antennas Propag.*, vol. 62, no. 4, pp. 1681-1689, Apr. 2014.

[28] F. Viani, G. Oliveri, and A. Massa, "Compressive sensing pattern matching techniques for synthesizing planar sparse arrays," *IEEE Trans. Antennas Propag*., vol. 61, no. 9, pp. 4577-4587, Sept. 2013.

[29] P. Rocca, M. A. Hannan, M. Salucci, and A. Massa, "Single-snapshot DoA estimation in array antennas with mutual coupling through a multi-scaling BCS strategy," *IEEE Trans. Antennas Propag*., vol. 65, no. 6, pp. 3203-3213, Jun. 2017.

[30] M. Carlin, P. Rocca, G. Oliveri, F. Viani, and A. Massa, "Directions-of-arrival estimation through Bayesian Compressive Sensing strategies," *IEEE Trans. Antennas Propag*., vol. 61, no. 7, pp. 3828-3838, Jul. 2013.

[31] M. Carlin, P. Rocca, G. Oliveri, and A. Massa, "Bayesian compressive sensing as applied to directions-of-arrival estimation in planar arrays," *J. Electromagn. Waves Appl.*, vol.2013, pp.1-12, 2013 (DOI :10.1155/2013/245867).